State-to-state inelastic scattering of Stark-decelerated OH radicals with Ar atoms

Ludwig Scharfenberg,[a] Jacek Kłos,[b] Paul J. Dagdigian,[c] Millard H. Alexander,[d] Gerard Meijer[a] and Sebastiaan Y. T. van de Meerakker*[a]

The Stark deceleration method exploits the concepts of charged particle accelerator physics to produce molecular beams with a tunable velocity. These tamed molecular beams offer interesting perspectives for precise crossed beam scattering studies as a function of the collision energy. The method has advanced sufficiently to compete with state-of-the-art beam methods that are used for scattering studies throughout. This is demonstrated here for the scattering of OH radicals ($X^2\Pi_{3/2}$, $J = 3/2$, f) with Ar atoms, a benchmark system for the scattering of open-shell molecules with atoms. Parity-resolved integral state-to-state inelastic scattering cross sections are measured at collision energies between 80 and 800 cm^{-1}. The threshold behavior and collision energy dependence of 13 inelastic scattering channels is accurately determined. Excellent agreement is obtained with the cross sections predicted by close-coupling scattering calculations based on the most accurate *ab initio* OH + Ar potential energy surfaces to date.

I. Introduction

The detailed understanding of interactions between individual atoms and/or molecules is of fundamental importance in physical chemistry, and is pivotal to the interpretation of the dynamic behavior of macroscopic systems. The study of collisions between neutral atoms and molecules in the gas-phase is a well-established experimental avenue to probe the potential energy surfaces (PESs) that govern molecular interactions.[1]

The crossed molecular beam technique is ideally suited to obtain detailed information on the PES, and enables the study of molecular encounters under single collision conditions and in complete isolation from the environment. The level of detail that can be reached in these experiments depends on the uniqueness of the pre-collision conditions and on the quality of the detection method to analyze the scattering products. Gaining ever better control over the relevant parameters has thus been a recurrent theme in crossed beam experiments.

A wide variety of sophisticated methods have been developed to control the collision energy,[2,3] the internal quantum states,[4–6] the velocity spreads,[7,8] and the mutual orientation[9,10] of the scatterers. Powerful laser-based detection techniques have been developed to measure the state, angular and translational energy distribution of the scattering products.[11–14] Many of these methods have recently yielded new insights in molecular scattering processes, ranging from the role of nonadiabatic dynamics in elementary reactions[15,16] to product pair correlations in bimolecular reactive scattering.[17] In concert with

advances in the theoretical analysis of scattering processes, the wealth of available experimental scattering data has contributed enormously to our present understanding of how intermolecular potentials control molecular reaction dynamics.

Further enhancement of this relationship requires experiments with an increasing level of resolution and detail. In crossed beam experiments the most serious roadblock to further improve the resolution are the molecular beam pulses. A precise level of control over molecules in a beam has become possible with the Stark deceleration technique.[18] A Stark decelerator for neutral polar molecules is the equivalent of a linear accelerator (LINAC) for charged particles,[19] and exploits the interaction of a polar molecule with inhomogeneous time-varying electric fields. Compared to conventional molecular beam sources, a Stark decelerator produces beams of molecules with a narrow velocity spread, perfect quantum state purity, and with a computer-controlled velocity that can be tuned between standstill and high velocities. These monochromatic molecular beams offer the possibility of studying molecular encounters under well controlled and unexplored conditions, and offer new prospects to probe molecular interaction potentials with unprecedented detail.[20]

The application of Stark-decelerated beams in scattering experiments is still in its infancy, however. In 2006, Gilijamse *et al.* performed the thus far only state-to-state scattering experiment using a Stark decelerated molecular beam.[21] A Stark-decelerated beam of OH radicals was crossed with a conventional beam of xenon atoms, and the state-to-state rotational inelastic scattering cross sections were measured for a number of scattering channels as a function of the collision energy. This experiment clearly demonstrated the feasibility of the approach; however, the sensitivity of the experiment was limited by the rather low number densities of the decelerated molecules.

To exploit fully the potential of Stark-decelerated beams in scattering experiments, sensitivity levels should be reached

[a] Fritz-Haber-Institut der Max-Planck-Gesellschaft, Faradayweg 4-6, 14195 Berlin, Germany. E-mail: basvdm@fhi-berlin.mpg.de
[b] Department of Chemistry and Biochemistry, University of Maryland, College Park, MD 20742-2021, USA
[c] Department of Chemistry, The Johns Hopkins University, Baltimore, Maryland 21218-2685, USA
[d] Department of Chemistry and Biochemistry and Institute for Physical Science and Technology, University of Maryland, College Park, MD 20742-2021, USA

that comply with the standards in the field. During the last years, we have developed a new Stark decelerator that employs the so-called $s = 3$ mode of operation to eliminate the loss of molecules that occurs in decelerators of earlier designs. With this apparatus, packets of molecules can be produced with a superior number density, a narrower velocity spread, and a higher quantum state purity.[22] This Stark decelerator enables state-to-state scattering experiments with a sensitivity that is comparable to (or even exceeds) the level of sensitivity that is obtained in state-of-the-art crossed beam scattering experiments of similar systems. This we demonstrate here for the OH ($X\,^2\Pi$)–Ar system.

Rotational inelastic scattering of free radical species such as OH,[23,24] CH[25] and NO[26] with rare gas atoms have always been of special interest in crossed beam scattering experiments. This interest stems from the crucial roles that these species play in many areas of chemistry and physics, ranging from combustion to astrophysics. Because of the unpaired electrons, these radicals have non-zero electronic spin and orbital angular momentum. This renders more complex the rotational energy level structure. In addition, the scattering is dominated by collisions on two (or more) PESs. A detailed understanding of these elementary systems therefore provides a firm basis to understand the dynamics of more complex systems.

The OH($X\,^2\Pi$)–Ar system [together with the similar NO($X\,^2\Pi$)–Ar system] has emerged as the paradigm for the scattering of open shell radicals with rare gas atoms. In a series of crossed beam experiments, ter Meulen and coworkers prepared the OH radicals in the upper Λ-doublet component of the $X\,^2\Pi_{3/2}$, $J = 3/2$ level by hexapole state selection.[27,28] Accurate parity-resolved integral state-to-state cross sections for rotational excitation up to the $X\,^2\Pi_{3/2}$, $J = 9/2$ and the $X\,^2\Pi_{1/2}$, $J = 5/2$ states were obtained at high collision energies. Preferred excitation to one of the Λ-doublet states of the final rotational and spin–orbit state was observed, in agreement with the general propensity rules that follow from a formal quantum analysis.[29,30] Steric asymmetries of the inelastic cross sections were measured by orienting the OH radicals with either the O-end or the H-end towards the Ar atom by a static electric field in the collision zone.[31] The collision induced reorientation of the OH radicals was measured by probing the Stark-split states of the products corresponding to different orientations.[32] Under thermal bulk conditions, the evolution of oriented or aligned OH ($X\,^2\Pi$) radicals was studied in collisions with argon by polarization spectroscopy.[33,34] Detailed information on the OH($X^2\Pi$)-Ar PES has also been obtained from spectroscopic study of the bound states of the OH-Ar van der Waals complex.[35,36]

Here we report the investigation of rotational energy transfer of fully state-selected OH ($X\,^2\Pi_{3/2}$, $J = 3/2$, f) radicals in collisions with Ar atoms at collision energies between 80 and 800 cm^{-1}. Parity-resolved integral state-to-state scattering cross sections for rotational excitation up to the $^2\Pi_{3/2}$, $J = 9/2$ and the $^2\Pi_{1/2}$, $J = 5/2$ states are accurately measured. The collision energy dependence of the relative integral inelastic scattering cross sections, the threshold behavior of the inelastic channels, and the energy dependence of the state-resolved

propensities are accurately determined. Excellent agreement is obtained with cross sections determined by quantum close-coupled calculations based on recent high-quality *ab initio* OH-Ar PES's.

II. Experiment

A. Experimental setup

The production, Stark deceleration and detection of OH radicals as used in our experiment has been described in detail before.[22] We summarize the most relevant aspects in this section. The details that are relevant to the variation of the collision energy are given in section II B and II C.

A schematic overview of the experimental setup is shown in Fig. 1. A pulsed supersonic beam of OH radicals is produced by photolysis (193 nm) of nitric acid seeded in an inert carrier gas. During the expansion, nearly all molecules cool to the lowest rotational ($J = 3/2$) and vibrational level of the $X\,^2\Pi_{3/2}$ electronic ground state. This level consists of two Λ-doublet components (labelled e and f,[37] see part c of Fig. 2) that are separated in energy by only 0.05 cm^{-1}. Both components are therefore equally populated in the beam, but only the energetically higher lying f-component is low field seeking in inhomogeneous electric fields and can be Stark-decelerated. The lower e-component is high field seeking and is deflected from the beam axis in the experiment.

After passage through a 2 mm diameter skimmer, the beam enters the 2.6 meter long Stark decelerator that consists of 317 parallel pairs of high-voltage electrodes. Successive pairs are alternately charged or grounded, creating a periodic field along the beam axis.[38] Two distinct field configurations are produced by either charging the electrode pairs on the even or the odd numbered positions. The OH radicals can be decelerated or accelerated by switching back and forth between these two configurations using a sequence of high voltage
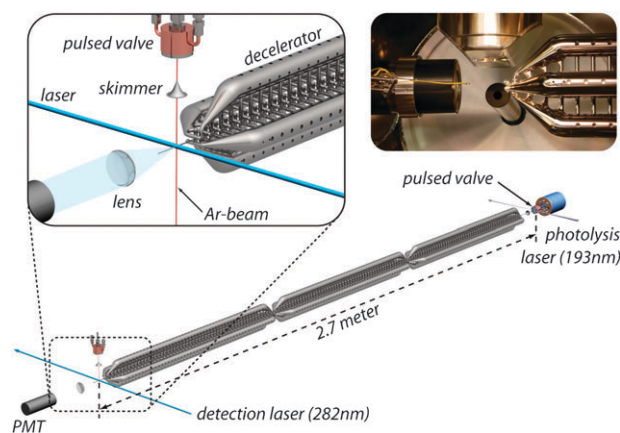

Fig. 1 Scheme of the experimental setup. A pulsed beam of OH radicals is produced *via* photodissociation of HNO$_3$ seeded in an inert carrier gas. The OH radicals pass through a 2.6-m-long Stark decelerator, and are scattered with a pulsed beam of argon atoms. The OH radicals are state-selectively detected using a laser-induced fluorescence scheme. The fluorescence is imaged onto a PMT. In the inset, a photograph of the beam crossing region is shown.
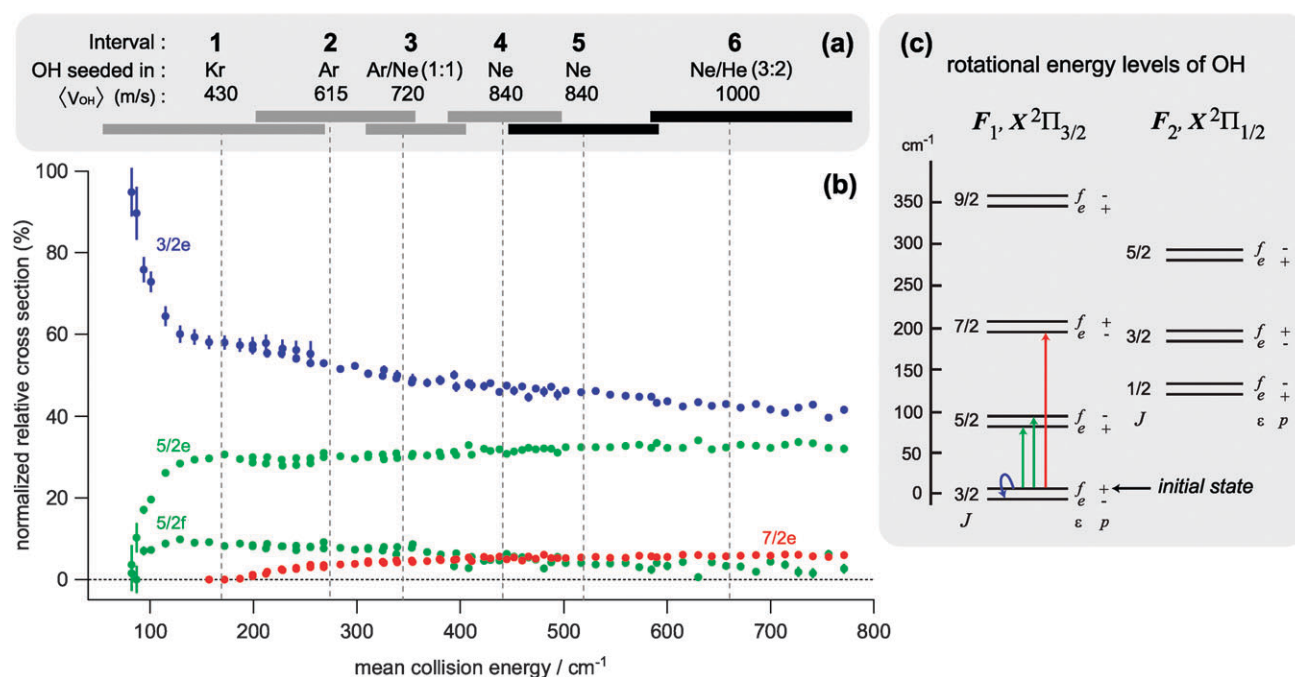
Fig. 2 (a) Collision energy intervals that were used to measure the collision energy dependence of the state-to-state scattering cross sections. The carrier gases that are used to generate OH radical beams with the indicated mean velocities are given above each interval. (b) Measured relative collision induced populations for the four strongest scattering channels, as indicated in the rotational energy level diagram of the OH radical (c). In this diagram, the energy splitting between both parity components is greatly exaggerated for reasons of clarity.

pulses. Essential in our experiments is the use of the so-called $s = 3$ operation mode of the decelerator.[39] In this mode, only every third electrode pair is used for deceleration, while extra transverse focusing is provided by the intermediate electrode pairs.

The packet of OH ($X\,^2\Pi_{3/2}$, $J = 3/2$, f) molecules that emerges from the decelerator intersects with the central axis of the beam of argon atoms at a distance of 16.5 mm from the exit of the decelerator under 90° angle of incidence. The fields are switched off when the OH radicals leave the decelerator, and collisions take place in a field free region. We assume that the uneven distribution over M_J-components that is present in the decelerator is scrambled completely before collisions occur. A modified commercial solenoid valve (General Valve, Series 99) is used to produce the pulsed supersonic beam of argon. The velocity of this beam can be adjusted by controlling the temperature of the valve. The atoms pass a 2 mm diameter skimmer and intersect the centerline of the OH packet 90 mm from the nozzle orifice. The duration of the gas pulse is long, and the number density of the argon atoms in the crossing region is constant during the passage of the OH packet. Single collision conditions are insured by keeping the decrease of the population in the $J = 3/2$, f level due to scattering with the argon atoms below 4 percent. A microphone based beam detector[40] can be moved into the crossing region to probe the spatial density profile of the argon beam. Together with a second microphone that is placed 300 mm further downstream, the mean forward beam velocity is determined from a time of flight measurement of the gas pulse.

The OH radicals are state-selectively detected via saturated laser induced fluorescence when the most intense part of the OH packet is in the center of the beam crossing region. The 282 nm radiation of a pulsed dye laser intersects both beams under 90° angle of incidence, and induces rotational transitions of the $A\,^2\Sigma^+$, $v = 1 \leftarrow X\,^2\Pi$, $v = 0$ band. The off-resonant fluorescence is collected at right angles by a lens and imaged onto a photomultiplier tube (PMT). Stray light from the laser is suppressed by light baffles and by optical filtering in front of the PMT. The radiative lifetime of the $A\,^2\Sigma^+$, $v = 1$ state is 717 ns,[41] and no collisional quenching of the excited molecules takes place. The diameter of the laser beam is approximately 8 mm, providing a detection volume that is larger than the intersection volume of the OH and Ar beams.

B. Variation of the collision energy

The collision energy is varied by deceleration, guiding, or acceleration of the OH radicals in the Stark decelerator, and by using two different temperatures for the argon valve. The total energy range of 80 to 800 cm^{-1} is covered using six separate measurement intervals, as is illustrated in Fig. 2(a). The argon valve is operated at 110 K for the collision energy range of 80 to 500 cm^{-1} (intervals 1 to 4) and at 293 K for energies between 430 and 800 cm^{-1} (intervals 5 and 6). The corresponding argon beam velocities are determined to be 400 and 565 m s^{-1} and stagnation pressures of 2 and 4 bar were used. Lower temperatures for the valve are not possible without the risk of condensation.

For a given velocity of the argon beam, the collision energy range that is accessible by tuning the velocity of the OH radicals is defined by the initial velocity of the OH molecular

beam. Molecular beams are produced using Kr, Ar, Ne, a Ne/Ar mixture, and a He/Ne mixture as carrier gas; the gas that is used in each interval is indicated in Fig. 2(a) together with the mean initial velocity of the molecular beam pulse. The collision energies that correspond to these mean velocities are indicated by vertical lines in Fig. 2(a) for each interval. Within each interval, the argon beam velocity is fixed and the collision energy is continuously scanned from low to high energies by deceleration and acceleration of the OH radicals. The velocity range of the OH radicals was chosen to ensure overlap between successive intervals.

The number density, velocity spread, quantum state purity, and size of the OH packet critically depends on the carrier gas that is used, and on the final velocity of the OH radicals. Within a measurement interval, the number density varies by about a factor of three throughout the range of final velocities. The highest number densities are typically observed for final velocities that are close to the mean velocity of the initial molecular beam, and for beams that are produced with a light carrier gas. The velocity spread depends on the settings of the Stark decelerator, and ranges from 10 to 25 m s^{-1}. The size of the packet is confined in the direction perpendicular to the beam axis to the 3×3 mm^2 aperture of the Stark decelerator; the length of the packet in the beam direction depends on the settings of the decelerator and is typically 10–15 mm. The state purity of the OH packet strongly depends on the carrier gas that is used and the settings of the Stark decelerator. Representative values of the background populations in levels other than the $J = 3/2, f$ level are given in Table 1 for the different carrier gases that were used. The deceleration/acceleration process is highly quantum state specific, and the quantum state purity of the OH radicals approaches 100%. The quantum state purity only drops below 99% when helium or neon is used, which reflects the inferior rotational cooling of OH radicals during the supersonic expansion for He and/or Ne containing carrier gases. The contaminating population is mainly in the low-field seeking $X^2\Pi_{3/2}, J = 5/2, f$ level. Population in high-field seeking levels of e-parity is negligible for all experimental conditions.

The energy resolution depends on the velocity and angular spreads of both beams. The phase-space distribution of OH radicals that emerge from the decelerator is accurately known from simulations of the deceleration process. The spatial distribution of argon atoms is estimated from the microphone measurements; the velocity distribution is estimated to be 12% of the mean velocity. The collision energy distribution is approximately Gaussian with a full width at half maximum of 20 cm^{-1} at the lowest collision energies and grows approximately linearly to 33 cm^{-1} at 500 cm^{-1}.

C. Experimental procedure and data analysis

The experiment runs at a repetition rate of 10 Hz, and all relevant trigger pulses to synchronize the experiment are computer controlled. The argon beam runs at a repetition rate of 5 Hz, and the collision signals are inferred from the signal intensity difference of alternating shots of the experiment. Within each interval of collision energies, the collision energy is varied in a quasi-continuous cycle. The Stark decelerator is programmed to produce a different velocity of the OH radicals every second shot of the experiment. The timing of the argon valve is adjusted automatically to match the arrival time of the OH packet in the collision zone. The collision energy is scanned within an interval using typically 5–15 different velocities of the OH packet; a single scan is thus made in 1–3 s. This scan is cycled 1000 times for every scattering channel, and the scattering signals that correspond to the same collision energies are averaged. Such cycles are made for all inelastic channels, and for all collision energy intervals. This measurement procedure ensures that the collision energy dependence of a given inelastic channel is insensitive to long-term variations in either the beam intensities or the laser wavelength, and can be measured independently from other channels. The relative signal intensities for the inelastic channels are measured for a fixed collision energy in each interval separately. These reference points are measured a few times, and are used to scale the signal intensities that result from the automated cycles with respect to each other.

During all measurements, the fluorescence signals are recorded using dedicated data acquisition software. The signal intensity of the strongest and weakest scattering channels differs by three orders of magnitude, and two modes of signal processing are used. The weakest channels are analyzed using photon counting; an analog mode of detection is used for the strongest channels. Both modes of signal acquisition are calibrated with respect to each other by comparing both modes for several channels with intermediate signal intensity.

With the experimental arrangement used here, only scattering events that change the quantum state of the OH radical, *i.e.*, inelastic scattering events, can be studied. A total of 13 inelastic scattering channels are measured. These channels populate the rotational levels that are shown in the energy level diagram in Fig. 2(c). The rotational levels are referred to hereafter as $F_i(Je/f)$, where $i = 1$ and $i = 2$ are used to indicate the $X^2\Pi_{3/2}$ and $X^2\Pi_{1/2}$ spin–orbit manifolds, respectively, and the parity labels e and f correspond to the two Λ-doublet components of each rotational level. The rotational energies of all levels are given in Table 2, together with the rotational transitions that are used to probe the individual levels. The transitions are labelled using the nomenclature of Dieke and Crosswhite.[43] A number of rotational levels are probed by inducing both the main and satellite lines of a transition simultaneously. The laser intensity is carefully adjusted to saturate both the main and satellite lines, without causing spectral overlap between the transitions that probe individual levels.

To relate fluorescence signal intensities to collision induced populations, the fraction of molecules that are laser excited and that contribute to the fluorescence intensity must be taken into account. This fraction is referred to as the excitation

Table 1 Background population in %. All other states are populated to less than 0.04%

Carrier gas	$F_1(5/2f)$	$F_1(7/2f)$	$F_2(1/2f)$
Kr	0.10–0.40	—	—
Ar	0.17–0.43	—	—
Ar/Ne (1 : 1)	0.26–0.72	0.01–0.04	0.01–0.07
Ne	2.40–3.40	0.04–0.12	0.13–0.20
Ne/He (3 : 2)	1.83–2.90	0.02–0.15	0.12–0.22

Table 2 The rotational states of the OH radical that are of relevance to the experiment. The rotational energy of the levels, the rotational transitions that are used to probe the population in the levels, and the excitation rates that apply to these transitions are given. Rotational energies are adapted from ref. 42.

		e			f		
	J	Transition	ER	E/cm^{-1}	Transition	ER	E/cm^{-1}
F_1	$\frac{3}{2}$	P_1	$\frac{1}{3}$	[0.000]	$Q_1 + Q_{21}$	$\frac{3}{5}$	0.055
	$\frac{5}{2}$	P_1	$\frac{2}{5}$	83.723	Q_1	$\frac{1}{2}$	83.924
	$\frac{7}{2}$	P_1	$\frac{3}{7}$	201.931	Q_1	$\frac{1}{2}$	202.379
	$\frac{9}{2}$	P_1	$\frac{4}{9}$	355.120	Q_1	$\frac{1}{2}$	355.914
F_2	$\frac{1}{2}$	$Q_2 + Q_{12}$	$\frac{3}{4}$	126.296	P_{12}	$\frac{1}{2}$	126.453
	$\frac{3}{2}$	Q_2	$\frac{1}{2}$	187.497	$P_{12} + P_2$	$\frac{3}{5}$	187.757
	$\frac{5}{2}$	Q_2	$\frac{1}{2}$	288.776	P_{12}	$\frac{1}{2}$	289.048

rate (ER). We assume that for laser excitation under saturated conditions, the population in the rotational level that is probed is equilibrated between all possible M_J levels of the initial and final levels of the rotational transition.[25,28] Under this assumption, the ER is given by $g''/(g' + g'')$, where $g'' = (2J'' + 1)$ and $g' = (2J' + 1)$ denote the degeneracy of the initial and final state, respectively. In case molecules are excited by main and satellite lines simultaneously, g' is given by the sum over the degeneracies of the two final states. The excitation rates that apply to the rotational transitions to probe the 13 inelastic scattering channels are listed in Table 2. The population in selected rotational levels was probed using different optical transitions, and it was verified that the difference in fluorescence intensities reflect the difference in excitation rates. The laser radiation is linearly polarized, and it was verified that a rotation of the polarization axis does not influence the fluorescence intensities.

In Fig. 2(b) the measured relative collision induced populations are shown for the four strongest channels, *i.e.*, the channels that populate the $F_1(3/2e)$, $F_1(5/2e)$, $F_1(5/2f)$, and $F_1(7/2e)$ levels. The vertical error bars represent the statistical spread (2σ) of the data as obtained from repeated runs of the experiment. The $F_1(5/2e)$, $F_1(5/2f)$, and $F_1(7/2e)$ levels open at a collision energy of 83.7 cm^{-1}, 83.9 cm^{-1}, and 201.9 cm^{-1} respectively, and the energetic thresholds are clearly recognized in the data. The only exoenergetic inelastic channel is scattering to the $F_1(3/2e)$ level, and all inelastic scattering events populate this level at the lowest collision energies that were probed. We will postpone the discussion of all 13 measured channels to section IV; we will first describe the theoretical methods that were used to calculate the inelastic scattering cross sections.

III. Theory

When a diatomic molecule in a Π electronic state interacts with a spherical target, the degeneracy is lifted, giving rise to two states, one of A' and one of A'' symmetry, in which the singly occupied π orbital lies, respectively in, or perpendicular to, the triatomic plane.[44] The inelastic scattering can be described in terms of the average V_{sum} and half-difference V_{dif} of the potential energy surfaces (PESs) corresponding to these two states.[29,44]

A. Potential energy surfaces

In our simulations of the present experiments we used two sets of PESs. The first were the restricted-coupled-cluster [RCCSD(T)] PESs of Toboła *et al.*[33] Here, the ArOH complex is described by single-determinant restricted Hartree–Fock (RHF) wavefunction with the OH molecular geometry frozen at its equilibrium bondlength $r_e = 0.96966$ Å. Subsequently, a full single- and double-excitation coupled-cluster calculation was carried out with non-iterative inclusion of triple excitations [RCCSD(T)].[45] We used the augmented correlation-consistent, quadruple-zeta (aug-cc-pvqz) atomic orbital basis sets of Dunning and coworkers.[46,47] The analytic fit to this RCCSD(T) PES has already been used in scattering studies of the Ar–OH(X) system.[33] For the present investigation we also used a second set of PESs, in which we averaged the interaction potential over the $v = 0$ vibrational motion of the OH molecule. Here, we used a spin-unrestricted, coupled-cluster method [UCCSD(T)], which allows more flexibility in the description of the wave function of the system by introducing different spatial functions for α and β spin–orbitals. We used the MOLPRO 2008 program suite[48] to carry out UCCSD(T) calculations on a grid of points specified by, in Jacobi coordinates, 10 equi-spaced values of the Ar–OH angle θ [with $\theta = 0$ corresponding to collinear ArHO], 35 values of the Ar–OH distance ranging from 3.5 a_0 to 25 a_0, and five values of the OH bond distance r [0.7, 0.85, 0.96966, 1.15, 1.4 Å]. This range of values of r spans well the lower vibrational wavefunctions of the OH radical. The interaction energy is determined in a supermolecular, counterpoise corrected approach where the total energies of the dimer and of the monomers are calculated using a dimer centered basis set.[49] At each point on the grid we performed three calculations for the PESs of both the A' and A'' electronic states, using, successively, aug-cc-pvtz, aug-cc-pvqz and aug-cc-pv5z atomic orbital bases.[46,47] These were then extrapolated to the complete basis set limit, using the mixed exponential and Gaussian formula of Peterson *et al.*[50,51] Finally, the resulting three-dimensional V_{sum} and V_{dif} PES's were averaged over the $v = 0$ OH vibrational wavefunction. As shown in Fig. 2 of ref. 33, the ArOH PESs have minima in both collinear geometries. In addition, the state of A' reflection symmetry exhibits an additional minimum in bent geometry. The position and depth of these minima are listed in Table 3, as predicted by the present UCCSD(T) calculations as well as by the RCCSD(T)[33] and the earlier calculations of Kłos and co-workers,[52] based on the application of 4th-order Møller–Plesset perturbation theory within an unrestricted (spin-polarized) framework (UMP4). As can be seen, the differences between the three CCSD(T) PESs are very small. Averaging over the $v = 0$ vibrational motion of the OH moiety results in a slight (~ 1 cm^{-1}) lowering of the well depth and a small shift in the minimum.

B. Scattering calculations

The OH radical in its ground $X\,^2\Pi$ electronic state is split into a lower (labelled F_1) and upper (F_2) spin–orbit manifold.[53] In Hund's case (a) these correspond, for a molecule with a negative spin–orbit constant, such as OH, to projection quantum numbers of the sum of the electronic orbital and spin angular

10664 | *Phys. Chem. Chem. Phys.*, 2010, **12**, 10660–10670

This journal is © the Owner Societies 2010

Table 3 Calculated position and depth of the minima in the OH-Ar potential energy surface as predicted by four different *ab initio* surfaces.[a]

Method	θ_e	R_e	D_e
	ArHO, linear		
UMP4	0	7.08	147.3
RCCSD(T)	0	6.98	140.4
UCCSD(T)/CBS, $r = r_e$	0	6.97	141.0
UCCSD(T)/CBS, $\langle v = 0 \rangle$	0	7.01	141.7
	ArOH, linear		
UMP4	180	6.70	95.5
RCCSD(T)	180	6.71	91.8
UCCSD(T)/CBS, $r = r_e$	180	6.70	91.4
UCCSD(T)/CBS, $\langle v = 0 \rangle$	180	6.70	92.4
	ArOH, A', bent		
UMP4	135.5	6.23	75.1
RCCSD(T)	137.4	6.19	74.4
UCCSD(T)/CBS, $r = r_e$	136.4	6.19	73.9
UCCSD(T)/CBS, $\langle v = 0 \rangle$	137.1	6.18	74.8

[a] Angles in degree, distances in a_0, energies in cm^{-1}.

momenta $\Omega = 3/2$ and $\Omega = 1/2$, respectively. Each rotational level J is further split into two close-lying Λ-doublet levels, which are labelled e and f. For a state of doublet multiplicity, the total parity is $+(-1)^{J-1/2}$ for the e-labelled states and $-(-1)^{J-1/2}$ for the f-labelled states.[37] To define the asymptotic energies of the OH molecule we used the known spectroscopic values of the rotational constant in the lowest vibrational manifold ($B_0 = 18.5487$ cm^{-1}), the spin–orbit constant ($A_0 = -139.21$ cm^{-1}), and the two Λ-doubling parameters ($p = 0.235$ cm^{-1} and $q = -0.0391$ cm^{-1}).[54] We further assume that the value of the spin–orbit constant of the OH is not altered by approach of the Ar atom. We have used the HIBRIDON program suite[55] to carry out fully-quantum, close-coupling calculations[29] of integral cross sections for the scattering of $OH(X^2\Pi)$ with Ar on a dense grid of 3270 collision energies ranging from 0.2 to 2500 cm^{-1}. We used a channel basis large enough to ensure convergence of the integral and differential cross sections for all $J, F_i \rightarrow J'$, F_i' transitions with $J, J' \leq 11.5$. The rotational basis set of OH was increased gradually with increasing total energy up to a maximum value of $J = 14.5$. At each collision energy, the maximum value of the total angular momentum $\mathscr{J}$ was set large enough ($\mathscr{J}_{max}^{tot} = 280$ for collision energies between 2000–2500 cm^{-1}) that the inelastic cross sections were converged to within 0.01 $\mathring{A}^2$. We have also calculated differential cross sections, using both sets of PESs, for transitions from the initially prepared $F_1(3/2f)$ level. These cross sections, which were used in the calculation of the density to flux transformation (see the Appendix for further details), were computed on a coarser grid of collision energies.

IV   Results and discussion

The experimental scattering signals are most easily compared with theoretical calculations when relative inelastic scattering cross sections are analyzed. The measured relative collision induced populations do not yield directly the relative scattering cross sections, but must be corrected for the detection probability of the scattered molecules. This probability is not equal for all scattered molecules and depends mostly on the post-collision velocity of the OH radicals. Molecules with a low laboratory velocity reside longer in the detection area, and are thus detected with higher probability than high velocity products which leave the detection area quickly.

The detection probability of a scattered OH radical depends on kinematic factors such as the translational energy of the products and/or the differential cross section (DCS) of the scattering process, and on experimental geometric factors like the spatial and temporal distribution of the colliding molecular beams and the size of the detection laser beam. To obtain the relative scattering cross sections from the raw experimental data, we corrected the scattering signals using a model that is explained in detail in the Appendix. Only small corrections are needed for our experimental conditions, typically 0.1 to 5 percent. The correction factors are insensitive to small differences in the DCS. Use of DCS's from calculations based on the RCCSD(T) and UCCSD(T) sets of PESs gives rise to correction factors that are virtually identical.

The resulting experimental relative inelastic scattering cross sections for 13 inelastic channels are shown in Fig. 3. The cross sections for inelastic scattering generally rise sharply from the energy threshold, reach a maximum, and become rather insensitive to a variation of the collision energy at higher energies. For fine structure conserving collisions (transitions within F_1 spin–orbit manifolds) there is a strong propensity for final states of e-parity, while final states of f-parity are preferred for fine-structure changing collisions. An exception to this general propensity rule is the $F_2(1/2)$ state for which the e-component is preferred in collisional excitation. These propensities are consistent with previous state-to-state inelastic scattering studies at high collision energies, and are well understood.[28]

To facilitate a direct comparison between experiment and theory, we have also included in Fig. 3 the corresponding cross sections computed using the RCCSD(T) and UCCSD(T) PESs, as described in section III, convoluted with the experimental energy resolution. Excellent agreement is obtained for both potentials for all inelastic channels throughout the entire range of collision energies. Slightly better agreement is found for cross sections computed with the UCCSD(T) potential. However, the differences between cross sections computed for the two sets of PES's are minor. This reflects the minor differences between them, as illustrated by the comparison of well depths and separations in Table 3.

For fine-structure-conserving transitions to levels within the F_1 spin–orbit manifold we find excellent agreement between the experimental and computed cross sections. The only exceptions are slight differences for the transitions to the $F_1(3/2e)$ and $F_1(5/2e)$ levels for collision energies above 500 cm^{-1}. For a $^2\Pi$ molecule described well by Hund's case (a) [which is not, strictly speaking, the case for $OH(X)$] transitions within a given spin–orbit manifold are induced by the average (V_{sum}) of the PESs for A' and A'' symmetry.[29] Thus the good agreement between experiment and theory for fine-structure conserving transitions seen in Fig. 3 is a measure of the quality of the V_{sum} PES predicted by the CCSD(T) calculations.

Transitions from the F_1 to F_2 spin–orbit manifolds are induced [again, in the Hund's case (a) limit] by the difference

This journal is © the Owner Societies 2010

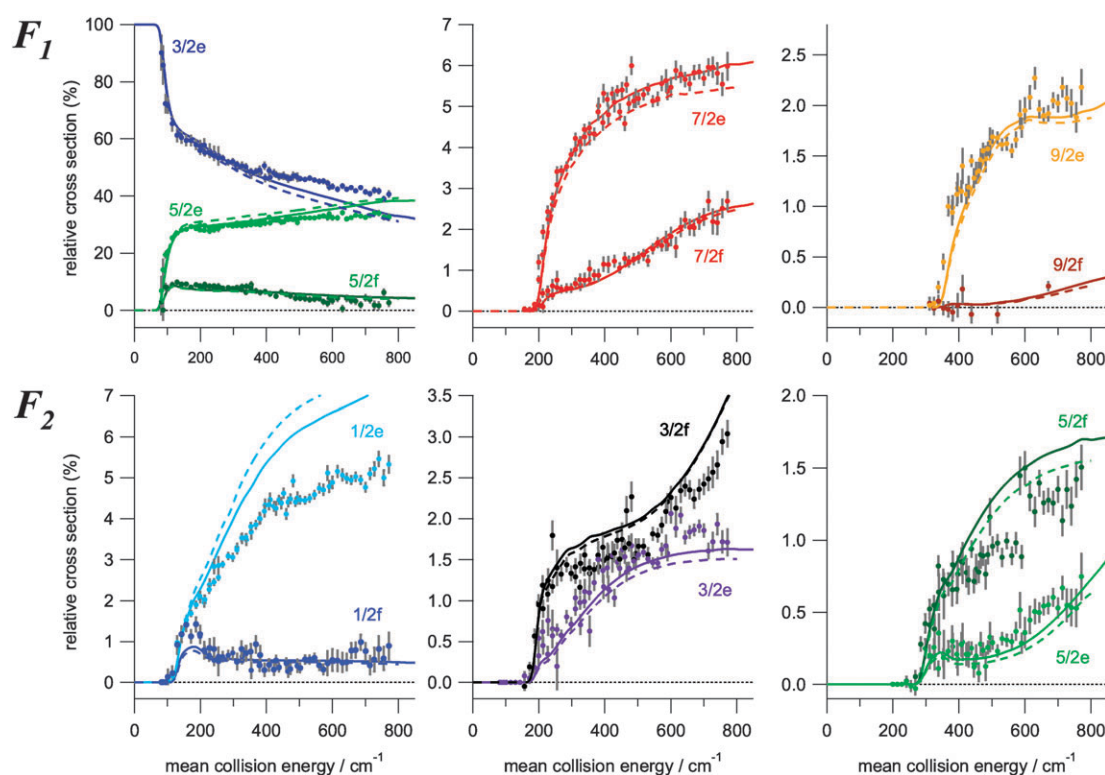*Phys. Chem. Chem. Phys.*, 2010, **12**, 10660–10670 | 10665

Fig. 3 Measured relative state-to-state inelastic scattering cross sections for the scattering of OH ($X^2\Pi_{3/2}$, $J = 3/2$, f) radicals with argon atoms as a function of the collision energy. The relative cross sections that result from the RCCSD(T) and the UCCSD(T) potential energy surfaces are given by the dashed and solid curves, respectively.

PES (V_{dif}).[29] The largest disagreement between experiment and theory occurs for transition to the $F_2(1/2e)$ level, for which the computed cross sections are significantly larger for collision energies greater than 200 cm^{-1}. We note, however, that these cross sections are considerably smaller in magnitude than those for the spin–orbit conserving transitions. None-theless, the disagreement of the cross sections for the transition to the $F_2(1/2e)$ level suggests that the difference between the A' and A'' *ab initio* Ar–OH(X) PESs may be less accurate than their average.

As can be seen in Fig. 3, the difference in the cross sections predicted by the earlier RCCSD(T) and the present UCCSD(T) calculations is small. In general, and in particular in the case of the transition into the $F_2(1/2e)$ level, this difference is considerably smaller than the magnitude of the disagreement between theory and experiment. The present UCCSD(T) PESs represent an average over the zero-point vibrational motion of the OH molecule. Comparison of these vibrationally averaged UCCSD(T) PESs with those calculated for the OH molecule frozen at $r = r_e$, the same rigid rotation approximation that was made in the RCCSD(T) calculations, show very little difference. The vibrationally averaged UCCSD(T) PESs, which are extrapolated to the complete basis set limit, represent the best currently achievable potential energy surfaces for a system like OH-Ar. Extending the complexity of the treatment of electron correlation to include full (rather than perturbative) inclusion of triple, and, ultimately, quadruple excitations would be computationally impractical.

We observe in Fig. 3 that the disagreement between theory and experiment increases at higher collision energy. At higher collision energy, the classical turning point moves up the repulsive wall. Thus, it is possible that the increasing discrepancy at higher energy indicates a progressively increasing inaccuracy higher on the repulsive wall. It is here, when the three atoms are closest, that a fully correct description of electron correlation becomes increasingly important. Thus, incompleteness in the description of triple excitations, and the neglect of quadruple excitations, may possibly lead to a greater degree of inaccuracy in the calculated PESs in the repulsive region.

Since the interaction of OH with Ar is known to support bound levels of the van der Waals complex,[35,56,57] resonances will appear in the energy dependence of the state-to-state cross sections arising from scattering into OH(J)Ar van der Waals states which lie below the OH(J) + Ar asymptote but can decay to OH(J' < J) + Ar. We present in Fig. 4 state-to-state cross sections for transitions from the $F_1(3/2f)$ level to the levels in the upper, F_2 fine-structure manifold. We see sharp structures in the energy dependence of the cross sections, which correspond to these resonances. Since the widths of these features are much narrower than the energy resolution of the experiment, these resonances can at present not be observed in the experimentally-measured cross sections. The experimental energy resolution is sufficient, however, to resolve broader structures in the cross sections. The theoretically predicted "hump" just above threshold in the cross section for excitation to the $F_2(1/2f)$ state, for instance, is reproduced well in the experiment.
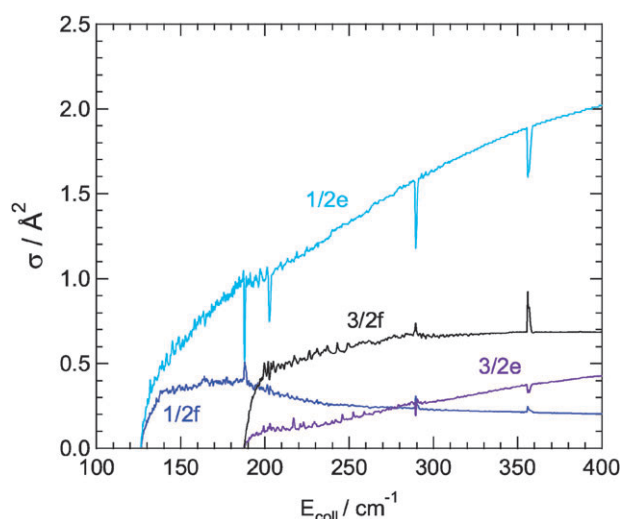
Fig. 4 State-to-state integral cross sections for transitions from the $F_1(3/2f)$ level to the two lowest rotational levels in the F_2 spin–orbit manifold as a function of the collision energy, computed with the UCCSD(T) PESs.

V Conclusions and outlook

We have presented measurements of the state-to-state rotational inelastic scattering of OH radicals as a function of the collision energy. The velocity and the initial quantum state of the OH radicals prior to the collision is controlled by passing the OH radicals through a Stark decelerator. The collision energy is varied from 80 to 800 cm^{-1}, and the relative inelastic scattering cross sections have been accurately determined for 13 inelastic scattering channels. Throughout the range of collision energies that were probed, excellent agreement is found with the results of quantum scattering calculations that are based on the most accurate PESs currently available. These PESs should provide a very good description of the interaction of the OH radical with Ar atoms.

The present experiment has allowed a more comprehensive comparison of experimental and theoretical inelastic cross sections than has been hitherto possible. The implications of the experiments that are presented in this Perspective reach beyond the OH-Ar system alone. These experiments also demonstrate that the Stark deceleration technique has matured sufficiently to be applied successfully in a wide range of scattering experiments.

The level of sensitivity that can now be achieved in these experiments is comparable to the sensitivity of conventional crossed beam experiments of similar systems. In the present experiment, the sensitivity allows for the observation of scattering processes with cross sections $\geq$ 0.01 Å^2. In future experiments one could add many of the well-established methods of the crossed beam experimentalist. For instance, the collision energy dependence of steric effects can be investigated by adding a static orientation field around the beam intersection region. The implementation of a velocity map imaging detector would allow for the measurement of the collision energy dependence of the differential cross sections.[11] The narrow velocity spread of the Stark decelerated beam yields images of the scattering products with a high angular and velocity resolution.

The Stark deceleration technique is applicable to a number of molecular species, and allows for scattering studies involving chemically relevant molecules like OH, NO, ND$_3$, H$_2$CO, and SO$_2$. The recent development of the related Zeeman deceleration technique extends this chemical diversity to molecules like NH and O$_2$, all molecular radical species, and all metastable atoms.[58,59]

The study of molecular collisions in the 1–20 cm^{-1} energy range is another exciting avenue. Cold molecular collisions are governed by rich quantum phenomena such as shape or Feshbach resonances that are less pronounced in collisions at high energies.[60,61] These resonances are extremely sensitive to the details of the interaction potential, but have thus far escaped experimental observation. Over the energy regime investigated here, molecular collisions are expected to be highly susceptible to externally applied fields, opening the possibility for controlled chemistry. The Stark deceleration technique offers viable routes to reach experimentally the required energy range and resolution. For instance, in the present experiment the angle between the reagent beams can be made smaller to further reduce the collision energy. Although more challenging, the scattering between *two* Stark-decelerated packets of molecules, either directly or in a molecular synchrotron, allows for the scattering between fully state-selected and velocity controlled molecules at collision energies down to 1 cm^{-1}.[20,62]

Although originally conceived as a method to produce cold polar molecules by decelerating molecules to a near-standstill, the Stark deceleration technique offers exciting perspectives for molecular beam scattering experiments as well. These tamed molecular beams add a novel new element to the existing collection of experimental methods to unravel the precise nature of molecular interactions.

VII Appendix

In crossed beam scattering experiments with pulsed molecular beams, only in exceptional cases can measured scattering signals be directly related to cross sections.[63] Generally, a so-called number density-to-flux transformation needs to be performed that requires information on the spatial and temporal distributions of the overlapping beams, the details of the detection system, and the differential cross section of the scattering process.[25,64,65]

The necessity to establish the relationship between measured scattering signals and inelastic scattering cross sections is illustrated in Fig. 5. In this Figure, the arrival time distribution of OH ($X^2\Pi_{3/2}, J$ = 3/2, f) radicals is shown that is recorded for settings of the experiment to produce a collision energy of 268 cm^{-1} (solid black curve). The packet of OH radicals is prepared with a velocity of 615 m s^{-1}, and has a mean arrival time of 4276 μs. The arrival time distribution that results from three dimensional trajectory calculations is shown as an overlay (dashed black curve). The scattering signals for four indicated rotational inelastic scattering channels are recorded for ten different detection times T. These scattering signals are normalized and shown in Fig. 5(a) as separate data points for each value of T. The relative inelastic scattering cross sections that are expected for these four channels from the UCCSD(T)

potential are given by the horizontal dashed curves. At early times, when the leading edge of the OH packet just overlaps with the Ar beam, the scattered molecules are still flocked together and are detected with equal probability. The measured relative scattering signals directly reflect the relative inelastic scattering cross sections. At a later time, the scattered molecules have dispersed into a larger area according to their post-collision laboratory velocity distributions. From this time on, scattered OH radicals that have a low laboratory speed accumulate in the interaction region and are detected more efficiently than scattered OH radicals with a large laboratory speed. Collisions that populate the F_1, $J = 3/2,e$ level, for instance, are strongly forward scattered and therefore less efficiently detected as T increases.

A model is developed to numerically calculate the fraction of inelastically scattered molecules that is detected for the conditions that apply to the present experiment. Consider a packet of OH radicals that is on collision course with the argon beam as illustrated schematically in part (b) of Fig. 5. We define the time $t = 0$ when the last electric field stage of the decelerator is switched off. The total number of molecules scattered into a final state j until a certain time t, $N_{sc}(j,t)$, is proportional to the integral inelastic cross section σ_j. The number of particles that are in state j and inside the detection volume at time t, $N_{det}(j,t)$, is likewise proportional to σ_j. Both particle numbers are related through a factor that we call the detection probability P_j

$$P_j = \frac{N_{det}(j,t)}{N_{sc}(j,t)}, \quad (1)$$

which is independent of the integral inelastic cross section σ_j. The detection probability is only unity for favorable conditions under which *all* scattered molecules are detected, *i.e.*, when the detection volume is large compared to the interaction volume of both beams and for sufficiently small values of t. In general, P_j depends on the laboratory velocity vectors of the scattered particles, and hence on the inelastic scattering channel that is probed.

In the model, the phase-space distribution of the OH radicals at the time $t = 0$ is simulated using numerical trajectory calculations.[66] The argon beam is assumed to have a Gaussian density distribution in the z-direction (corresponding to the molecular beam axis of the Stark decelerator), and a homogenous distribution in the x and y-directions. The argon density is assumed to be constant in time, and all OH radicals scatter with an argon atom with unit probability. The z-coordinate of the impact position is chosen randomly from the spatial distribution of the argon atoms; the x and y coordinates and time of impact t_{impact} then follow from the position and velocity coordinates of the OH radicals at time $t = 0$. The three velocity components of the colliding argon atom are chosen randomly from Gaussian velocity distributions.

The possible post-collision velocity vectors of the OH radical follow from energy and momentum conservation. Part (c) of Fig. 5 shows the Newton diagram for the experimental parameters mentioned above. The laboratory velocity vectors before the collision are denoted by $\mathbf{v}_{OH}$ and $\mathbf{v}_{Ar}$ for OH and Ar respectively, $\mathbf{v}_{cm}$ denotes the velocity of the center of mass. The velocity vector $\mathbf{v}_{OH}$ as seen from the center of mass frame is
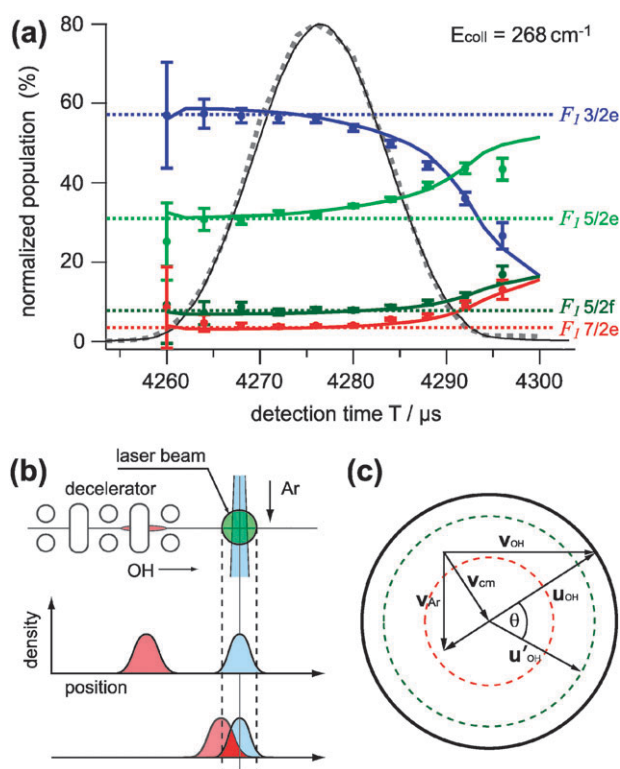

Fig. 5 (a) Measured (solid black curve) and simulated (dotted black curve) arrival time distribution of a packet of OH ($F_1(3/2f)$) radicals with a mean velocity of 615 m s^{-1}. The normalized collision induced populations into the $F_1(3/2e)$, $F_1(5/2e)$, $F_1(5/2f)$, $F_1(7/2e)$ levels are shown that are measured as a function of the detection time. The theoretically calculated relative inelastic scattering cross sections are shown as horizontal dashed lines. The relative collision induced populations that are obtained from a computer model of the collision and detection process are shown as solid curves. (b) A schematic of the geometry of the setup. (c) The Newton diagram for the experimental parameters of part (a): $v_{OH} = 615$ m s^{-1}, $v_{Ar} = 400$ m s^{-1}. The outer and inner dashed circles corresponds to rotational transitions to the $F_1(5/2e,f)$ and $F_1(7/2e,f)$ levels respectively.

denoted by $\mathbf{u}_{OH}$ before and by $\mathbf{u}'_{OH}$ after the collision. Both enclose the "scattering angle" θ. In the course of the collision $\mathbf{u}_{OH}$ changes in length because the collision is inelastic. If we denote the collision energy by E and the energy for the rotational transition by ΔE_{rot} the length of $\mathbf{u}'_{OH}$ is given by

$$u'_{OH} = u_{OH}\sqrt{\frac{E - \Delta E_{rot}}{E}}. \quad (2)$$

To specify the direction of $\mathbf{u}'_{OH}$, we use the standard convention in which θ ranges from $0°$ (forward scattering) to $180°$ (backward scattering). The angle that specifies the direction within the plane that is perpendicular to $\mathbf{u}_{OH}$ is denoted by ϕ, and all values for $0 \leq \phi \leq 2\pi$ are equally probable. The final velocity after the collision in the laboratory frame is given by $\mathbf{v}'_{OH} = \mathbf{v}_{cm} + \mathbf{u}'_{OH}$. The distribution in the scattering angle θ is denoted by $g(\theta)$ and can be determined from the differential cross section (DCS):

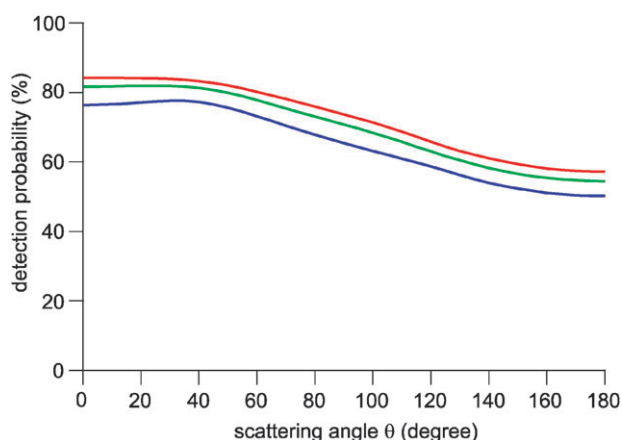$$g(\theta)d\theta = \frac{DCS(\theta)\sin(\theta)d\theta}{\int_0^\pi DCS(\theta)\sin(\theta)d\theta}. \quad (3)$$

Fig. 6 A plot of the detection probability $w_j(\theta)$ for three values of ΔE_{rot}, corresponding to scattering into the $F_1(3/2e)$ (blue curve), $F_1(5/2e,f)$ (green curve) and $F_1(7/2e,f)$ (red curve) rotational levels. The parameters that are used in this simulation apply to the experimental conditions of Fig. 5(a) and $T = 4276$ μs.

Instead of including the scattering angle distribution directly within the computer simulation, it is more convenient to first calculate the detection probability $w_j(t,\theta)$ as a function of the scattering angle and detection time. We define w_j by

$$w_j(t,\theta) = \frac{N_{det}(j,t,\theta)}{N_{sc}(j,t)}, \qquad (4)$$

where N_{det} is defined as before, but the scattering angle is now fixed and not distributed according to the function $g(\theta)$. The calculation of w is done for a given θ by propagating all molecules from the time t_{impact} to t and by counting the molecules found within the detection volume. For every particle, a new random value of ϕ is chosen. For each inelastic channel, $w_j(\theta)$ is calculated by repeating this procedure for values of θ between $0°$ and $180°$. The detection probability curves that are relevant to the inelastic scattering channels and collision energy of Fig. 5 are shown in Fig. 6. It is seen that the detection probability changes only moderately with the scattering angle.

The total detection probability for a specific state and for a detection time T is then given by

$$P_j(T) = \int_0^\pi w_j(T,\theta)g_j(\theta)\mathrm{d}\theta. \qquad (5)$$

The differential cross sections are obtained from the close-coupling calculations (see section III), and the detection probabilities $P_j(T)$ are calculated for every collision energy of the experiment, *i.e.*, for every setting of the Stark decelerator, and for all measured scattering channels.

The validity of the model can be verified by computing the time evolution of P_j. Referring back to Fig. 5, the scattering signals that are expected from the model at a collision energy of 268 cm^{-1} are shown as solid curves. Excellent agreement is obtained between the measured relative scattering signals and the model predictions. Similar measurements have been made at collision energies of 172, 438, and 517 cm^{-1}, and a good agreement with the model predictions was obtained for all

collision energies (data not shown). The ability to accurately reproduce the temporal dependence of the scattering signals for a range of scattering channels and collision energies yields high confidence in the validity of the model.

Acknowledgements

References

1 R. Levine and R. Bernstein, *Molecular Reaction Dynamics and Chemical Reactivity*, Oxford University Press, New York, 1987.
2 G. Hall, K. Liu, M. McAuliffe, C. Giese and W. Gentry, *J. Chem. Phys.*, 1983, **78**, 5260.
3 D. M. Sonnenfroh, R. G. MacDonald and K. Liu, *J. Chem. Phys.*, 1991, **94**, 6508.
4 G. A. Raiche, J. B. Jeffries, K. J. Rensberger and D. R. Crosley, *J. Chem. Phys.*, 1990, **92**, 7258.
5 J. Reuss in *Atomic and Molecular Beam Methods*, ed. G. Scoles, Oxford University Press, New York, NY, USA, 1988 and 1992, vol. 1 and 2, ch. 11, pp. 276–292.
6 S. Stolte in *Atomic and Molecular Beam Methods*, ed. G. Scoles, Oxford University Press, New York, NY, USA, 1988 and 1992, vol. 1 and 2, ch. 25, pp. 631–652.
7 C. J. N. van den Meijdenberg in *Atomic and Molecular Beam Methods*, ed. G. Scoles, Oxford University Press, New York, NY, USA, 1988 and 1992, vol. 1 and 2, ch. 13, pp. 345–361.
8 M. Faubel, K.-H. Kohl, J. P. Toennies, K. T. Tang and Y. Y. Yung, *Faraday Discuss. Chem. Soc.*, 1982, **73**, 205.
9 S. Stolte, *Nature*, 1991, **353**, 391.
10 D. Watanabe, H. Ohoyama, T. Matsumura and T. Kasai, *Phys. Rev. Lett.*, 2007, **99**, 043201.
11 H. Kohguchi, T. Suzuki and M. H. Alexander, *Science*, 2001, **294**, 832.
12 M. N. R. Ashfold, N. H. Nahler, A. J. Orr-Ewing, O. P. J. Vieuxmaire, R. L. Toomes, T. N. Kitsopoulos, I. A. Garcia, D. A. Chestakov, S.-M. Wu and D. H. Parker, *Phys. Chem. Chem. Phys.*, 2006, **8**, 26.
13 K. Liu, *Phys. Chem. Chem. Phys.*, 2007, **9**, 17.
14 N. E. Shafer-Ray, A. J. Orr-Ewing and R. N. Zare, *J. Phys. Chem.*, 1995, **99**, 7591.
15 L. Che, Z. Ren, X. Wang, W. Dong, D. Dai, X. Wang, D. H. Zhang, X. Yang, L. Sheng and G. Li, *et al.*, *Science*, 2007, **317**, 1061.
16 X. Wang, W. Dong, C. Xiao, L. Che, Z. Ren, D. Dai, X. Wang, P. Casavecchia, X. Yang and B. Jiang, *et al.*, *Science*, 2008, **322**, 573.
17 J. J. Lin, J. Zhou, W. Shiu and K. Liu, *Science*, 2003, **300**, 966.
18 S. Y. T. van de Meerakker, H. L. Bethlem and G. Meijer, *Nat. Phys.*, 2008, **4**, 595.
19 H. L. Bethlem and G. Meijer, *Int. Rev. Phys. Chem.*, 2003, **22**, 73.
20 S. Y. T. van de Meerakker and G. Meijer, *Faraday Discuss.*, 2009, **142**, 113.
21 J. J. Gilijamse, S. Hoekstra, S. Y. T. van de Meerakker, G. C. Groenenboom and G. Meijer, *Science*, 2006, **313**, 1617.
22 L. Scharfenberg, H. Haak, G. Meijer and S. Y. T. van de Meerakker, *Phys. Rev. A: At., Mol., Opt. Phys.*, 2009, **79**, 023410.
23 P. Andresen, D. Häusler and H. W. Lülf, *J. Chem. Phys.*, 1984, **81**, 571.

This journal is © the Owner Societies 2010

Phys. Chem. Chem. Phys., 2010, **12**, 10660–10670 | 10669

24 P. Andresen, N. Aristov, V. Beushausen and H. W. Lülf, *J. Chem. Phys.*, 1991, **95**, 5763.

25 R. MacDonald and K. Liu, *J. Chem. Phys.*, 1989, **91**, 821.

26 D. W. Chandler and S. Stolte, *Gas Phase Molecular Reaction and Photodissociation Dynamics*, Inelastic energy transfer: The NO-rare gas system, Transworld Research Network, 2007, pp. 1–63.

27 K. Schreel, J. Schleipen, A. Eppink and J. J. ter Meulen, *J. Chem. Phys.*, 1993, **99**, 8713.

28 M. C. van Beek, J. J. ter Meulen and M. H. Alexander, *J. Chem. Phys.*, 2000, **113**, 628.

29 M. H. Alexander, *J. Chem. Phys.*, 1982, **76**, 5974.

30 P. J. Dagdigian, M. H. Alexander and K. Liu, *J. Chem. Phys.*, 1989, **91**, 839.

31 M. C. van Beek, J. J. ter Meulen and M. H. Alexander, *J. Chem. Phys.*, 2000, **113**, 637.

32 M. C. van Beek, G. Berden, H. L. Bethlem and J. J. ter Meulen, *Phys. Rev. Lett.*, 2001, **86**, 4001.

33 G. Paterson, S. Marinakis, M. L. Costen, K. G. McKendrick, J. Kłos and R. Toboła, *J. Chem. Phys.*, 2008, **129**, 074304. Erratum: G. Paterson, S. Marinakis, M. L. Costen, K. G. McKendrick, J. Kłos and R. Toboła, *J. Chem. Phys.*, 2009, **131**, 159901.

34 P. J. Dagdigian and M. H. Alexander, *J. Chem. Phys.*, 2009, **130**, 094303.

35 R. T. Bonn, M. D. Wheeler and M. I. Lester, *J. Chem. Phys.*, 2000, **112**, 4942.

36 M. C. Heaven, *Int. Rev. Phys. Chem.*, 2005, **24**, 375.

37 J. M. Brown, J. T. Hougen, K. P. Huber, J. W. C. Johns, I. Kopp, H. Lefebvre-Brion, A. J. Merer, D. A. Ramsay, J. Rostas and R. N. Zare, *J. Mol. Spectrosc.*, 1975, **55**, 500.

38 H. L. Bethlem, F. M. H. Crompvoets, R. T. Jongma, S. Y. T. van de Meerakker and G. Meijer, *Phys. Rev. A: At., Mol., Opt. Phys.*, 2002, **65**, 053416.

39 S. Y. T. van de Meerakker, N. Vanhaecke, H. L. Bethlem and G. Meijer, *Phys. Rev. A: At., Mol., Opt. Phys.*, 2005, **71**, 053409.

40 J. G. Choi, J. S. Hayden, M. T. O'Connor and G. J. Diebold, *J. Appl. Phys.*, 1981, **52**, 6016.

41 D. R. Yarkony, *J. Chem. Phys.*, 1992, **97**, 1838.

42 J. A. Coxon, *Can. J. Phys.*, 1980, **58**, 933.

43 G. H. Dieke and H. M. Crosswhite, *J. Quant. Spectrosc. Radiat. Transfer*, 1962, **2**, 97.

44 M. H. Alexander, *Chem. Phys.*, 1985, **92**, 337.

45 P. J. Knowles, C. Hampel and H.-J. Werner, *J. Chem. Phys.*, 1993, **99**, 5219. Erratum: P. J. Knowles, C. Hampel and H.-J. Werner, *J. Chem. Phys.*, 2000, **112**, 3106.

46 T. H. Dunning, Jr., *J. Chem. Phys.*, 1989, **90**, 1007.

47 R. A. Kendall, T. H. Dunning, Jr. and R. J. Harrison, *J. Chem. Phys.*, 1992, **96**, 6796.

48 H.-J. Werner, P. J. Knowles, R. Lindh, F. R. Manby, M. Schütz, and others, MOLPRO, version 2008.1, a package of *ab initio programs*, see http://www.molpro.net.

49 F.-M. Tao and Y.-K. Pan, *J. Chem. Phys.*, 1992, **97**, 4989.

50 K. A. Peterson, D. E. Woon and T. H. Dunning, Jr., *J. Chem. Phys.*, 1994, **100**, 7410.

51 D. Feller and J. A. Sordo, *J. Chem. Phys.*, 2000, **112**, 5604.

52 J. Klos, G. Chalasinski, M. T. Berry, R. A. Kendall, R. Burcl, M. M. Szczesniak and S. M. Cybulski, *J. Chem. Phys.*, 2000, **112**, 4952.

53 G. Herzberg, *Spectra of Diatomic Molecules*, Van Nostrand, Princeton, 1968.

54 J. P. Maillard, J. Chauville and A. W. Mantz, *J. Mol. Spectrosc.*, 1976, **63**, 120.

55 HIBRIDON is a package of programs for the time-independent quantum treatment of inelastic collisions and photodissociation written by M. H. Alexander, D. E. Manolopoulos, H.-J. Werner and B. Follmeg, and others. More information and/or a copy of the code can be obtained from the website http://www.chem.umd.edu/groups/alexander/hibridon/hib43.

56 M. T. Berry, R. A. Loomis, L. C. Giancarlo and M. I. Lester, *J. Chem. Phys.*, 1992, **96**, 7890.

57 Y. Endo, H. Kohguchi and Y. Ohshima, *Faraday Discuss.*, 1994, **97**, 341.

58 N. Vanhaecke, U. Meier, M. Andrist, B. H. Meier and F. Merkt, *Phys. Rev. A: At., Mol., Opt. Phys.*, 2007, **75**, 031402.

59 M. G. Raizen, *Science*, 2009, **324**, 1403.

60 R. C. Forrey, N. Balakrishnan, V. Kharchenko and A. Dalgarno, *Phys. Rev. A: At., Mol., Opt. Phys.*, 1998, **58**, R2645.

61 N. Balakrishnan, A. Dalgarno and R. C. Forrey, *J. Chem. Phys.*, 2000, **113**, 621.

62 C. E. Heiner, D. Carty, G. Meijer and H. L. Bethlem, *Nat. Phys.*, 2007, **3**, 115.

63 G. Hall, K. Liu, M. J. McAuliffe, C. F. Giese and W. R. Gentry, *J. Chem. Phys.*, 1984, **81**, 5577.

64 D. M. Sonnenfroh and K. Liu, *Chem. Phys. Lett.*, 1991, **176**, 183.

65 Ch. Naulin, M. Costes, A. Benseddik and G. Dorthe, *Laser Chem.*, 1988, **8**, 283.

66 S. Y. T. van de Meerakker, N. Vanhaecke and G. Meijer, *Annu. Rev. Phys. Chem.*, 2006, **57**, 159.